

Simulating the Pyrolysis of Polyazides: a Mechanistic Case Study of the $[P(N_3)_6]^-$ Anion

Carmen Domene,^{*,†} Peter Portius,^{*,‡} Patrick W. Fowler,[‡] and Leonardo Bernasconi[§]

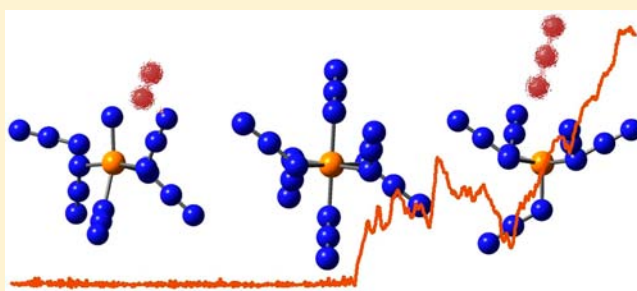
[†]Chemistry Research Laboratory, University of Oxford, Mansfield Road, Oxford OX1 3TA, U.K.

[‡]Department of Chemistry, University of Sheffield, Sheffield S3 7HF, U.K.

[§]Science and Technology Facilities Council, Rutherford Appleton Laboratory, Harwell Science and Innovation Campus, Didcot OX11 0QX, U.K.

S Supporting Information

ABSTRACT: Pyrolysis of the homoleptic azido complex $[P(N_3)_6]^-$ was simulated using density functional theory based molecular dynamics and analyzed further using electronic-structure calculations in atom-centered basis sets to calculate the geometries and electronic structures. Simulations at 600 and 1200 K predict a thermally induced and, on the simulation time scale, irreversible dissociation of an azido anion. The ligand loss is accompanied by a barrierless (free-energy) transition of the geometry of the complex coordination sphere from octahedral to trigonal bipyramidal. $[P(N_3)_5]$ is fluxional and engages in pseudorotation via a Berry mechanism.



INTRODUCTION

Nitrogen-rich molecules often contain large amounts of energy, which is released by the formation of hot N_2 gas during percussion-, friction-, or heat-induced decomposition. Several classes of “energy-storage compounds” are known, of which perhaps the most prominent are tetrazoles and azides. Major advances in the field have been made recently with the preparation and isolation of homoleptic polyazides of the type $E(N_3)_4$, where $E = C$,¹ Si ,² $[E(N_3)_4]^-$, where $E = B$,³ Al , and Ga ,⁴ $[E(N_3)_6]^-$, where $E = P$,⁵ As ,⁶ and Sb ,⁷ and $[E(N_3)_6]^{2-}$, where $E = Si$,⁸ Ge ,⁹ Sn ,¹⁰ Pb ,¹¹ Se ,¹² and Te .^{13,14} It has been found that the polyazido complex anions are generally more stable than the corresponding neutral complexes. This phenomenon has been ascribed to hypercoordination, thermodynamic effects induced by lattice energies, and a dilution of the reactive nitrogen content owing to the presence of large cations.⁵

Pyrolysis of alkyl azides has already been studied in both experiment and theory and tertiary alkyl azides,¹⁵ HN_3 ,¹⁶ and CH_3N_3 ^{16–18} and N_2 , H_2 , and HCN are observed as final products.¹⁹ The extrusion of nitrogen is predicted by CAS-SCF and CAS/MP2 calculations as the first step in the decomposition of alkyl azides.^{20,21} Pyrolysis of the related species HN_3 affords singlet and triplet nitrene,^{22,23} via spin-allowed and -forbidden reactions, respectively.

Recently, a new salt of the nitrogen-rich hexakis(azido)-phosphate anion, $[(PPh_3)_2N][P(N_3)_6]$, has been prepared and its decomposition studied by thermal analysis, mass spectrometry, and spectroscopy.⁵ Molecules containing covalent P–N bonds are generally difficult to isolate and handle²⁴ because of their highly endothermic character and very low free-energy

reaction barriers, which can often cause uncontrolled explosive decomposition. However, the energetic salt $[(PPh_3)_2N][P(N_3)_6]$ was found to be comparatively stable, with the onset of thermal decomposition at 515 K. From thermal measurements and mass spectrometric data, it was concluded tentatively that $[P(N_3)_6]^-$ is in equilibrium with $P(N_3)_5$ and N_3^- at temperatures above 500 K. However, the precise decomposition pathway and the identity of the species that lead to the ultimate liberation of N_2 are unknown; it is known from experimental results that the first step in the thermolysis of simple monoazides involves nitrogen elimination to yield the respective imine as the unique product.^{25–27} Other studies have treated polyazides, e.g., $Si(Ph)(N_3)_3$,²⁸ but have not investigated the mechanism. Thermal stability is essential in the viability assessment of not only nitrogen-rich species but especially all-nitrogen species. In this context, we note that mechanistic studies of the all-nitrogen systems $N_5^+/N_5^{-29,30}$ and N_5^+/N_3^{-31} have also been undertaken. Unraveling the mechanism of thermal decomposition of an exemplary polyazido complex, such as $[P(N_3)_6]^-$, is crucial for many purposes, i.e., understanding the energy-storing capabilities of these types of complexes,^{32,33} determining the properties that control their kinetic stability, and finding ways to control the energy release, safe energy-storage materials, and uses in organic reactions³⁴ and nitride synthesis.^{35–37} The factors that govern the stability of the polyazido complexes have received little attention, and mechanistic studies of the decomposition have, to the best of our knowledge, not been reported. The aim

Received: June 2, 2012

Published: January 28, 2013

of this study is to examine the mechanism of pyrolysis of the $[\text{P}(\text{N}_3)_6]^-$ anion using ab initio molecular dynamics (AIMD) and electronic-structure calculations.

METHODS

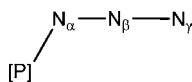
1. AIMD Calculations. Density functional theory (DFT)-based Born–Oppenheimer molecular dynamics (BO MD) simulations were performed using the Becke exchange³⁸ and Lee–Yang–Parr³⁹ correlation functionals. All calculations were carried out with the freely available Car–Parrinello molecular dynamics (CPMD) package.⁴⁰ The valence electrons were described in a plane-wave basis with an energy cutoff of 90 Ry. The interactions between valence electrons and ionic cores were described by analytical Goedecker–Teter–Hutter^{41,42} pseudopotentials. The accuracy of the pseudopotential representation chosen was assessed by a comparison with the various static properties of the system obtained in an all-electron calculation. The equilibrium temperature for most simulations was set to 600 K (controlled using a Nosé thermostat⁴³ at 60 cm^{-1}) and in one simulation to 1200 K. The $[\text{P}(\text{N}_3)_6]^-$ molecule was embedded in a cubic cell with 16 Å sides. Electrostatic decoupling of the periodic images was effected using Hockney’s method.⁴⁴ Long-range electrostatic interactions were treated with the Ewald method. These calculations and those described below were performed for gas-phase species; we are interested in the initial steps of decomposition, during which the counterion, owing to its bulk and inertness, is unlikely to interfere. It is known that with appropriate counterions, such as $[(\text{PPh}_3)_2\text{N}][\text{P}(\text{N}_3)_6]$, decomposition of $[\text{P}(\text{N}_3)_6]^-$ is accompanied by the release of N_3^- . The final stage of decomposition of $[(\text{PPh}_3)_2\text{N}][\text{P}(\text{N}_3)_6]$ is thermolysis of $[(\text{PPh}_3)_2\text{N}]\text{N}_3$.⁵

The various types of computation that were performed using AIMD are as follows:

(1) Two extensive unconstrained AIMD simulations at 600 K of duration ~ 25 and ~ 24 ps were run with time steps of 0.24 and 0.48 fs, respectively. The third AIMD simulation at 1200 K was carried out with a time step of 0.24 fs.

(2) In order to follow changes in the free energy, a series of AIMD calculations were performed, in each of which a bond length, d , connecting either P and N_α or N_α and N_β (see Scheme 1) was

Scheme 1. End-On Coordination of the Azido Ligand via the N_α Atom



constrained to a fixed value and time steps of 0.24 fs. AIMD simulations of duration ~ 10 and ~ 20 ps, respectively, with a time step of 0.24 fs were performed for $d_{\text{P}-\text{N}_\alpha}$ ranging from 1.7 to 2.0 Å and $d_{\text{N}_\alpha-\text{N}_\beta}$ ranging from 1.2 to 1.4 Å. The width of each window was 2.4 ps, and half of this simulation time was discarded as an equilibration period.

For each run, the mean force of the constraint, $f(d)$, was evaluated from the unbiased time average of the Lagrange parameter $\langle \lambda \rangle_d$ obtained by solving the equations of motion of the system with the imposed constraint⁴⁵ $f(d) = \langle \lambda \rangle_d - 2k_{\text{B}}T/d$, where k_{B} is Boltzmann’s constant and T the absolute temperature. For each run, the system was propagated until the mean force was sufficiently converged. Each new run was continued from the final atomic configuration of the previous one, by increasing the value of the constrained distance, d , and allowing sufficient time for thermal equilibration at the new value. The potential of the mean force (free energy) was then estimated numerically relative to its value in the reference state by integration. In this way, changes in the free energy were evaluated, and finite-temperature relaxation of the molecule was accounted for.

(3) Geometry optimizations of selected geometries arising in AIMD simulations were also carried out with the CPMD package. A maximum gradient cutoff of 5×10^{-4} au was used. Functional, pseudopotential, cutoff, and box dimensions were the same as those for the previous AIMD runs.

2. Electronic-Structure Calculations in Atom-Centered Basis Sets.

(1) In tandem with the thermodynamic integration calculations performed using plane-wave basis functions, a parallel approach was undertaken using all-electron wave functions in atom-centered basis sets to map the potential energy surface. A scan of the two reaction paths was performed to identify saddle points. This is a robust approach for finding a transition state, although it may typically require a large number of calculations. In the present case, each path has only one reaction coordinate to sample (the internuclear distance between P and N_α or between N_α and N_β). The scans were performed with sets of 10–19 points. At each value of the distance chosen as the reaction coordinate, full optimization of all other structural parameters for all three levels of electronic-structure theory listed under (2) was carried out.

(2) All-electron gas-phase calculations were performed with the *Gaussian09* package.⁴⁶ Geometries were optimized at the BLYP, B3LYP, B2PLYP, M06HF, Hartree–Fock (HF), and MP2 levels of theory using standard 6-311G(d,p) basis sets and characterized by computing the harmonic vibrational frequencies. The projected harmonic frequencies (see the Supporting Information, SI) include either no imaginary frequency (NIMAG = 0) or one (NIMAG = 1) with wavenumber values of $i(-464 \text{ cm}^{-1})$ to $i(-660 \text{ cm}^{-1})$ (B3LYP),

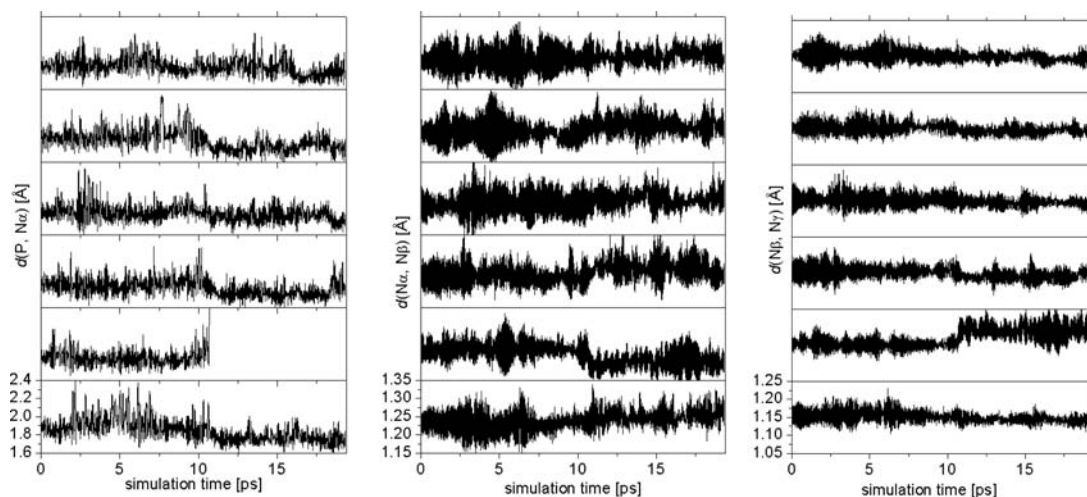


Figure 1. Plots of the internuclear distances $d(\text{P}-\text{N}_\alpha)$ (left), $d(\text{N}_\alpha-\text{N}_\beta)$ (middle), and $d(\text{N}_\beta-\text{N}_\gamma)$ (right) in the simulation with a time step of 0.48 fs and $T = 600$ K. Rows refer to the azido ligands a–f (top to bottom; see Scheme 1).

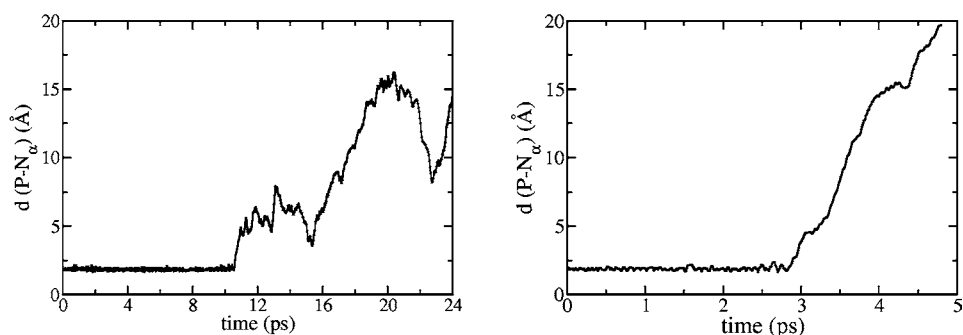


Figure 2. Plots of the distance $d(\text{P}-\text{N}_\alpha)$ of the azido ligand e in simulations with a time step of 0.48 fs at 600 K (left) and 1200 K (right).

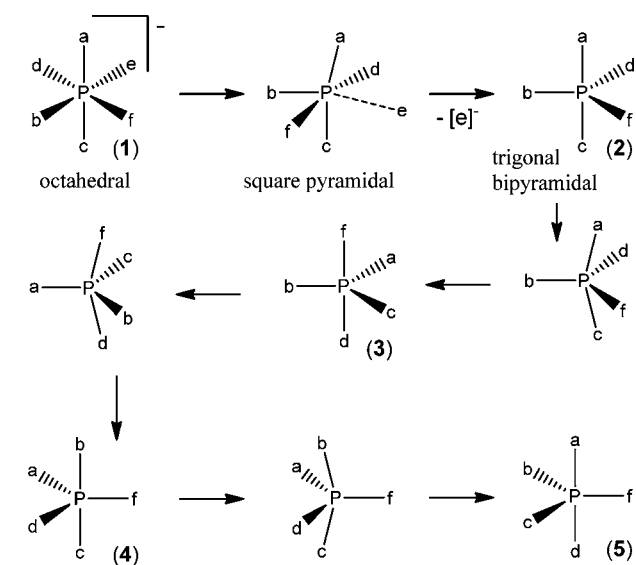
where $i = (-1)^{1/2}$, which correspond to the mode that, locally at least, leads downhill in one phase to reactants and in the other phase to products. All rigid-body motions correspond to wavenumbers of less than 7.5 cm^{-1} in magnitude (B3LYP), even for the largest systems treated. All geometry optimizations were performed using the Gaussian default fine grid. For minima, no imaginary frequencies were found (NIMAG = 0), while for transition states, one and only one such frequency was found (NIMAG = 1). Because the HF results are qualitatively similar to those obtained with DFT, they are reported in the SI only. The energies of dissociation reactions were corrected for basis set superposition error (BSSE).

RESULTS AND DISCUSSION

1. AIMD Simulations. The calculated interatomic distances of all $\text{P}-\text{N}_\alpha$, $\text{N}_\alpha-\text{N}_\beta$, and $\text{N}_\beta-\text{N}_\gamma$ bonds are shown as functions of time in simulations with a time step of 0.48 fs at 600 K (Figures 1 and 2; see Figures S3–S5 in the SI for plots of the simulation at 600 K with a time step of 0.24 fs). The temporal evolution of these distances shows only thermally induced oscillations ($1.58\text{--}2.41 \text{ \AA}$, $\text{P}-\text{N}_\alpha$; $1.14\text{--}1.37 \text{ \AA}$, $\text{N}_\alpha-\text{N}_\beta$; $1.09\text{--}1.34 \text{ \AA}$, $\text{N}_\beta-\text{N}_\gamma$) around their respective equilibrium values [$1.83(7)\text{--}1.93(12)$, $1.23(3)\text{--}1.24(3)$, and $1.15(2)\text{--}1.16(2) \text{ \AA}$], until after a $\sim 10.6 \text{ ps}$ simulation time, when one $\text{P}-\text{N}_\alpha$ bond breaks (involving ligand e; see Figure 2). The $\text{P}-\text{N}_\alpha$, $\text{N}_\alpha-\text{N}_\beta$, and $\text{N}_\beta-\text{N}_\gamma$ bonds vibrate with the main components of approximately 1.4×10^{13} , 3.7×10^{13} , and $5.8 \times 10^{13} \text{ s}^{-1}$, respectively, which correspond to the $\text{P}-\text{N}$ and symmetric and antisymmetric N_3 bond-stretching vibrations.

The initial elongation of the $\text{P}-\text{N}_\alpha$ bond results in a reduction of the symmetry of the coordination sphere from O_h to C_{4v} . A further modification of the symmetry is observed when the $\text{P}-\text{N}_\alpha$ bond breaks, with the result that the $\text{P}(\text{N}_3)_5$ fragment adopts a trigonal-bipyramidal coordination geometry. During this process, there is a gradual overall reduction in the average $\text{P}-\text{N}_\alpha$ [$1.77(8)\text{--}1.83(9) \text{ \AA}$] and $\text{N}_\beta-\text{N}_\gamma$ [$1.14(1)\text{--}1.15(1) \text{ \AA}$] bond lengths, and an elongation of the $\text{N}_\alpha-\text{N}_\beta$ bonds [$1.24(2)\text{--}1.26(2) \text{ \AA}$] in ligands a–d and f, while $d(\text{N}_\alpha-\text{N}_\beta)$ and $d(\text{N}_\beta-\text{N}_\gamma)$ of the former ligand e equalize [$1.20(2)$ and $1.19(2) \text{ \AA}$]. As the ligand e is escaping from the coordination center, the $\text{N}_\alpha-\text{P}-\text{N}_\alpha$ angles involving the ligands b, d, and f adjust to 120° . Subsequently, the coordination framework adopts the angles $171(2)^\circ$, $90(3)^\circ$, and $120(4)^\circ$ and is best described as trigonal-bipyramidal $\text{P}(\text{N}_3)_5$ (Scheme 2; the AIMD average bond lengths are given in Table S16 in the SI). While the $\text{N}_\alpha-\text{P}-\text{N}_\alpha$ bond angles of $[\text{P}(\text{N}_3)_6]^-$ oscillate within comparably narrow margins of $72\text{--}109^\circ$ (cis) and $155\text{--}180^\circ$ (trans), the $\text{N}_\alpha-\text{P}-\text{N}_\alpha$ angles in the new $\text{P}(\text{N}_3)_5$ fragment fall into three sets, two of which fluctuate with much larger amplitude: $79\text{--}115^\circ$ (f and c), $70\text{--}169^\circ$ (a and b; a and d; b and f; b and d; c and d), and $74\text{--}180^\circ$ (a and c; a and f; b and

Scheme 2. Schematic Representation of the Changes of Geometry in $[\text{P}(\text{N}_3)_6]^-$ during and after Dissociation of the Azido Ligand e on the Trajectory with a Time Step of 0.48 fs at 600 K



c; d and f). This behavior is a consequence of the configurational interconversions of axial (ax) and equatorial (eq) azido ligands, which occur three times in this simulation, at 16.1, 16.4, and 18.4 ps (Figure 3). The interconversions proceed via a transition state with square-pyramidal coordination geometry ($\text{N}_{\text{bas}}-\text{P}-\text{N}_{\text{bas}}$ (trans), $157(4)^\circ$; $\text{N}_{\text{bas}}-\text{P}-\text{N}_{\text{bas}}$ (cis), $88(5)^\circ$; $\text{N}_{\text{ap}}-\text{P}-\text{N}_{\text{bas}}$, $101(6)^\circ$; see Scheme 2 and Tables S1–S6 in the SI for full geometry, in the fashion of a *Berry pseudorotation*.⁴⁷ The Berry mechanism was suggested previously to be operational in the case of the valence isoelectronic binary polyazide $[\text{Te}(\text{N}_3)_4]$.⁴⁸

As can be seen from the angular changes, the respective pivot elements b, a, and f connect the four configurations 2–5 (see Scheme 2) via clockwise (2 \rightarrow 3 and 4 \rightarrow 5) or anticlockwise (3 \rightarrow 4) pseudorotations. At each stage, the coordination sites of four ligands change in the fashion ax \rightarrow eq \rightarrow eq \rightarrow ax (a), eq \rightarrow eq \rightarrow ax \rightarrow eq (b), ax \rightarrow eq \rightarrow ax \rightarrow eq (c), eq \rightarrow ax \rightarrow eq \rightarrow ax (d), and eq \rightarrow ax \rightarrow eq \rightarrow eq (f). As a result, the relative configuration of only one pair of ligands (c and f) remains unchanged (ax and eq) throughout, while a and b; a and d; b and f; b and d; and c and d change between ax and eq and between eq and eq and a and c; a and f; b and c; and d and f change involving all possible relative configurations (ax and

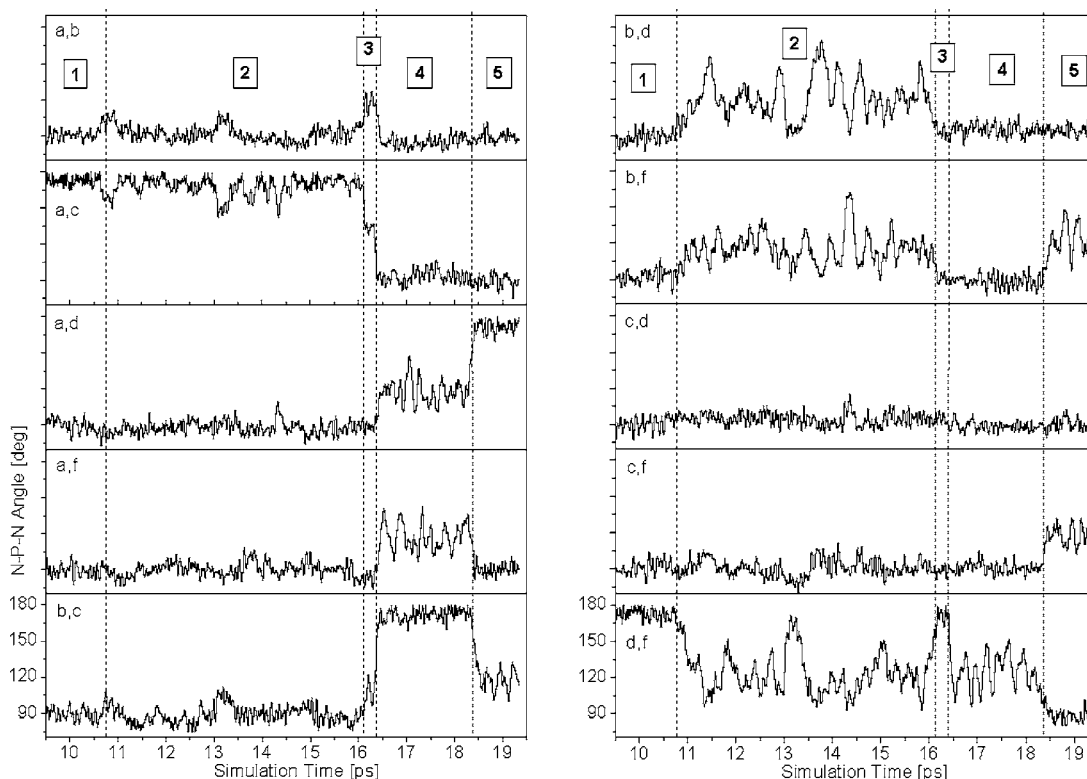


Figure 3. Plot of the 10 N_α -P- N_α angles involved in the fragment $P(N_3)_5$, with the azido ligands a, b, c, d, and f in the simulation with a time step of 0.48 fs and $T = 600$ K. The intervals 1–5 refer to Scheme 2.

ax; ax and eq; and eq and eq), thus rationalizing the observed fluctuation of the N_α -P- N_α angles.

In the interval between 10.6 and 13.2 ps simulation time, the azido ligand e escapes the complex, with P- N_α distances up to 7.9 Å (see Figure 1). During the following 2.3 ps, the ligand is partially “recaptured” and the P- N_α (e) distance falls until at 15.5 ps the sum of the van der Waals radii of P and N (3.55 Å) is reached. However, instead of reentering the coordination sphere, the former ligand escapes again in a rebound-like fashion. Analysis of the N_α -P- N_α angles indicates that the N_α atom of the free ligand e is prevented from further approach to the coordination center by the repulsive action of the ligands d and f in close vicinity, which include an angle of ca. 120° with P and are in the same plane with e.

The AIMD simulation of the $[P(N_3)_6]^-$ anion under identical conditions and start geometry but with a reduced time step of 0.24 fs shows a similar behavior; ligand d instead of ligand e dissociates from the complex at an earlier time of ~8.7 ps (ligands d and e are symmetry-equivalent). Within the margins of uncertainty caused by molecular vibration, all average bond lengths (9.0–12.5 ps) as well as bond angles of both N_3 and $P(N_3)_5$ fragments are indistinguishable from those observed with a time step of 0.48 fs between 11.2 and 15.7 ps. Both near-recapture of the N_3 fragment and pseudorotations are observed in the simulation with the shorter time step of 0.24 fs (see Figure 2).

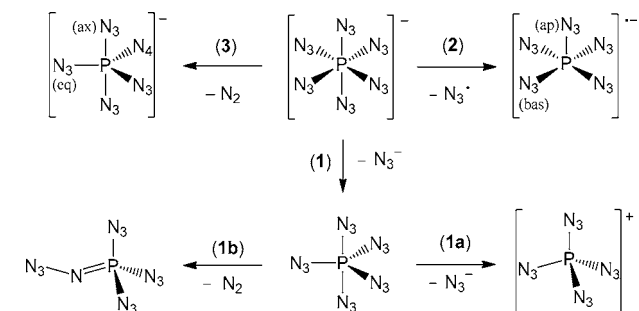
A simulation carried out at higher temperature (1200 K) under identical conditions and start geometry with a time step of 0.24 fs shows one ligand dissociating from the complex at an earlier time of just ~3 ps (see the SI). Both rebound of the N_3 fragment and pseudorotations are again observed after dissociation has taken place. A further simulation performed at very high temperature (3000 K) shows within the thermal

equilibration phase the successive release of two N_3 ligands (4000 steps) and one N_2 fragment (6000 steps) and the formation of a residual $P(N)(N_3)_3$ fragment (see the SI).

2. Analysis of the Observed AIMD Structures. The optimized geometries of differently charged $P(N_3)_5$ and N_3 fragments were inspected in order to identify the species with the best match to the geometries obtained from the AIMD simulations. The AIMD geometry of a fragment was estimated by taking coordinates of representative structures *before* ($[P(N_3)_6]^-$) and *after* the bond breaking events at 10.6 ps on the trajectory with a time step of 0.48 fs and at 8.6 ps on the trajectory with a time step of 0.24 fs (both 600 K).

In order to compare the results of the simulations with a putative initial N_2 elimination and dissociation into penta-(azido)phosphorane and an azido anion (Scheme 3, path 1), the homolytic cleavage of one P- N_α bond (path 2) and the

Scheme 3. Reaction Paths 1–3 Evaluated for Initiating the Pyrolysis of $[P(N_3)_6]^{-\alpha}$



$^{\alpha}$ ax = axial, eq = equatorial, ap = apical, and bas = basal.

Table 1. Energies (Electronic) of the Possible Products of the Pyrolysis Reaction of $[P(N_3)_6]^-$ Calculated at the B3LYP, BLYP, B2PLYP, RM06HF, and MP2 Levels of Theory Using Gaussian and the 6-311G(d,p) Basis Set^a

<i>n</i>	system	B3LYP (au)	BLYP (au)	B2PLYP (au)	RM06HF (au)	MP2 (au)
6	$[P(N_3)_6]^-$	-1326.8987	-1326.8135	-1325.9629	-1326.5342	-1323.9899
5	$[P(N_3)_4(N_4)]^-$	-1217.3550	-1217.2808	-1216.4993	-1217.0177	-1214.6909
	$[P(N_3)_5]^{*-}$	-1162.6264	-1162.5631	-1161.8111	-1162.2909	-1160.0695 ^b
	$[P(N_3)_5]$	-1162.5499	-1162.4780	-1161.7458	-1162.2471	-1160.0380
	$[P(N_3)_5]^{*+}$	-1162.2431	-1162.1706	-1161.4300	-1161.9159	-1159.7088
4	$[P(N_3)_3(N_4)]$	-1053.0277	-1052.9649	-1052.3040	-1052.7532	-1050.7605
	$[P(N_3)_4]^-$	-998.4114	-998.3569	-997.5132	-998.1388	-996.2780
	$[P(N_3)_4]^*$	-998.2880	-998.2359	-997.6065	-998.0190	-996.1138 ^b
	$[P(N_3)_4]^+$	-998.0578	-997.9993	-997.3860	-997.8140	-995.9442
3	$[P(N_3)_3]^{*-}$	-833.7668	-834.0992	-833.5830	-833.9198	-832.3721 ^b
	$[P(N_3)_3]$	-834.0941	-834.0497	-833.5472	-833.8905	-832.36438
	$[P(N_3)_3]^{*+}$	-833.7668	-833.7300	-833.2208	-833.5572	-832.0260
2	$[P(N_3)_2]^-$	-669.8863	-669.8507	-669.4635	-669.7347	-668.5412
	$[P(N_3)_2]^*$	-669.8291	-669.7937	-669.4054	-669.6700	-668.4682 ^b
	$[P(N_3)_2]^+$	-669.5494	-669.5228	-669.1353	-669.3999	-668.2238
-	N_3^-	-164.2622	-164.2478	-164.1246	-164.1912	-163.8529
-	N_3^*	-164.1812	-164.1711	-164.0421	-164.0986	-163.7644
-	N_2	-109.5559	-109.5441	-109.4714	-109.5319	-109.2970

^aNo symmetry constraints were applied. Selected BSSE-corrected relative energies [ΔG (kcal mol⁻¹), B3LYP/6-311G(d,p)] for the possible products of the pyrolysis reaction of $[P(N_3)_6]^-$ can be found in Table S14 in the SI. ^bSingle-point MP2 energy using the geometry of B3LYP/6-311G(d,p).

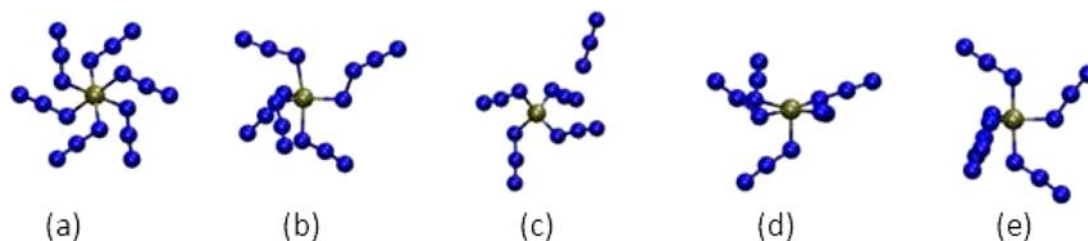


Figure 4. Ball-and-stick diagrams of the structures presented in Table 1 as obtained from B3LYP/6-311G(d,p) level of theory calculations: (a) $[P(N_3)_6]^-$; (b) $[P(N_3)_4(N_4)]^-$; (c) $[P(N_3)_5]^+$ (one P– N_α bond is not drawn because the P– N_α distance is greater than the standard length of a single bond); (d) $[P(N_3)_5]^{*-}$; (e) $[P(N_3)_5]$.

cleavage of one N_α – N_β bond and nitrogen elimination (path 3) as primary reactions and several secondary reactions were investigated. The energetics of the primary (path 2) and secondary (paths 1a and 1b, vide infra) reactions were analyzed by comparing a series of $[P(N_3)_n]^m$ complexes ($n = 2-6$, $m = 1-, 0, 1+$). Optimized structures of the complexes were obtained by using all-electron methods at the BLYP, B3LYP, B2PLYP, MP2 and M06HF/6-311G(d,p) levels of theory (Table 1 and Figure 4; for additional HF results, see the SI). The minimum character of each stationary point in the optimizations was verified by inspection of the computed harmonic vibrational frequencies. In agreement with predictions of the VSEPR model, the all-electron calculations found a trigonal-bipyramidal coordination sphere for $[P(N_3)_5]$ shown in Scheme 3 and Figure 4 (Table S16 in the SI compares the bond lengths in the phosphorus species with those found in the fragments of the AIMD simulations after the dissociation event).

All-electron calculations were also carried out on the azido anion N_3^- and penta(azido)phosphorane, $[P(N_3)_5]$. The equilibrium distances and angles obtained for the $D_{\infty h}$ symmetric N_3^- (1.184 Å and 180°) and the trigonal-bipyramidal penta(azido)phosphorane $[P(N_3)_5]$ (see the Table S16 in the SI) were within the limits defined by the standard deviations of the average interatomic distance in the

N_3 and $P(N_3)_5$ fragments in the AIMD simulations after dissociation [N_3 : 1.193 (± 0.011) Å, in the trajectory with a time step of 0.24 fs; 1.196 (± 0.013) Å, in the trajectory with a time step of 0.48 fs (600 K); for $P(N_3)_5$, see Table S16 in the SI).

Intervention of open-shell species $[P(N_3)_5]^{*-}$ (Figure 4d) and N_3^* (see ref 49 for a previous spectroscopic and theoretical study on this species) cannot occur in these simulations because the AIMD approach used does not allow for unpaired electrons. The reliability of the AIMD/CPMD/Gaussian comparison was tested on the starting complex, $[P(N_3)_6]^-$, where average distances (in Å) were found to be P– $N_\alpha = 1.88(3)$, 1.85, and 1.87 Å, N_α – $N_\beta = 1.23(1)$, 1.23, and 1.23 Å, and N_β – $N_\gamma = 1.16(0)$, 1.15, and 1.15 Å from AIMD, CPMD, and Gaussian optimizations (at the BLYP level of theory), respectively.

3. Energetics. Calculation of the dissociation (Helmholtz) free energy along a reaction coordinate corresponding to two interatomic distances, d_{P-N_α} and $d_{N_\alpha-N_\beta}$ was performed by pointwise thermodynamic integration of the mean constraint force, as described above. For these simulations, the distance $d_{N_\alpha-N_\beta}$ of one of the ligands was increased in steps of 0.05 Å from 1.20 to 1.60 Å. Beginning at the constrained distance of 1.35 Å, one other N_3 ligand dissociates spontaneously (for

$d_{N_\alpha-N_\beta} = 1.35 \text{ \AA}$ at a simulation time of 6 ps). A plot of the six average P– N_α distances with $d_{N_\alpha-N_\beta} = 1.60 \text{ \AA}$ exemplifies this situation by showing repeated dissociation and reassociation of one equatorial N_3 ligand (see Figures S6 and S8 in the SI). Therefore, an estimation of the free energy for the release of N_2 alone was not possible. In the simulations where the distance d_{P-N_α} was modified in six steps from 1.70 to 2.00 \AA (see Figure S7 in the SI), no subsequent release of N_2 was observed. However, at long constrained distances of 1.95 and 2.00 \AA , the dissociation of another N_3 ligand was noted. A Helmholtz free-energy change of ca. 2.4 kcal mol⁻¹ is required for pushing $[P(N_3)_6]^-$ up to a distance of 2.00 \AA on the P– N_α reaction coordinate of the N_3 dissociation path at 600 K.

In order to gain further insight into the relative energetics of the reactions, total energy profiles were calculated with *Gaussian09* for the closed-shell system $[P(N_3)_6]^-$. For these profiles, one P– N_α or P– N_β distance was varied with optimization of the rest of the structure at each stage (Scheme 3, path 1). A similar calculation was performed with the N_α – N_β distance of one azido ligand (Scheme 3, path 3). To check for dependence on the functional and method, optimizations were carried out using DFT (B3LYP, B2PLYP, and BLYP), HF (see the SI), MP2, and the exchange-correlation functional M06HF.⁵⁰ Figures 5 and 7 show a selection of the Gibbs

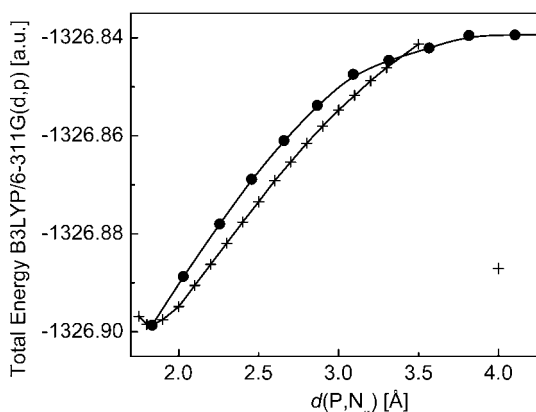


Figure 5. Potential energy profiles plotted as functions of the $d(P-N_\alpha)$ reaction coordinate in the system $[P(N_3)_6]^-$ at the B3LYP/6-311G(d,p) level of theory, obtained by stepping up the constraint $d(P-N_\alpha)$ (+) or $d(P-N_\beta)$ (●). The data point (+) at 4.00 \AA indicates a permutation of N_α and N_β on the $d(P-N_\alpha)$ reaction coordinate.

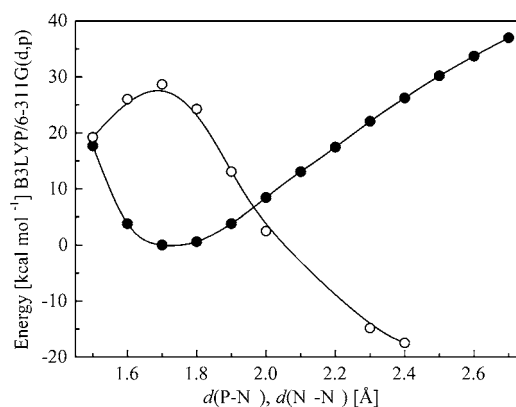


Figure 7. Potential energy profiles of the system $\text{tbp-}[P(N_3)_5]$ with respect to the reactant state in kcal mol⁻¹ at the B3LYP/6-311G(d,p) level of theory, obtained by stepping up the constraints $d(P-N_\alpha)$ (●) and $d(N_\alpha-N_\beta)$ (○).

energy profiles. Several observations can be made. (i) The dissociation of one N_3^- anion from $[P(N_3)_6]^-$ results in a monotonic increase of the total energy up to P– N_α distances [curves differ slightly depending on the constrained parameter $d(P-N_\alpha)$ and $d(P-N_\beta)$]. Despite the expected energy release resulting from rearrangement of the $P(N_3)_5$ fragment during later stages in the dissociation of the complex, no significant energy barrier was found for the reverse reaction. The rearrangement involves the gradual adjustment of the coordination geometry from square pyramidal (spy) to trigonal bipyramidal (tbp). (ii) The change of the total energy along the P– N_α reaction coordinate between the equilibrium distance and 2.00 \AA is on the order of magnitude found in the pointwise thermodynamic integration of the mean constraint force obtained from the simulations. (iii) The dissociation products on the P– N_α reaction coordinate were identified as neutral $P(N_3)_5$ and anionic N_3^- by comparison with the geometries of the independently optimized fragments (Figure 4e and the SI). The total energy increases by 54 kcal mol⁻¹ (B3LYP) or 60 kcal mol⁻¹ (RM06HF) when N_3^- is removed to infinity. (iv) The elimination of N_2 has an activation barrier of approximately 47 and 43 kcal mol⁻¹ (B3LYP and BLYP, respectively). The N_α atom left behind inserts into an adjacent P– N_α bond, forming an unusual η^1 -coordinating, chainlike N_4 ligand as part of the new complex $[P(N_3)_4(N_4)]^-$; see Table 1 and Figure 4b. Elimination and insertion proceed synchronously with a net

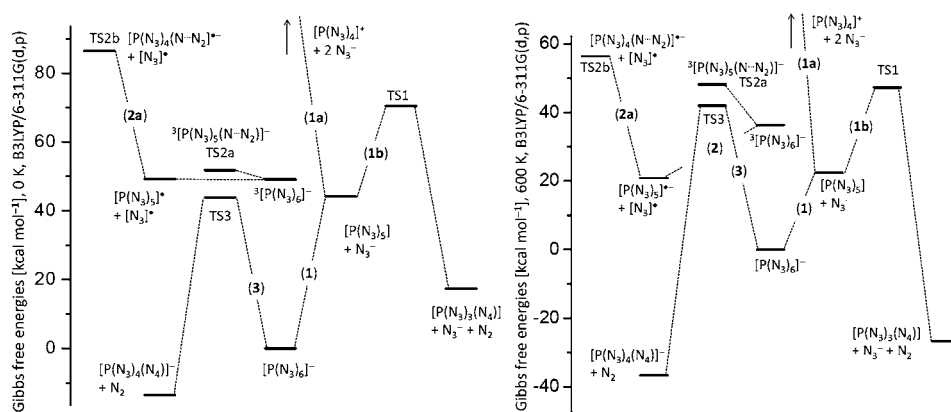


Figure 6. Energy diagrams of $[P(N_3)_6]^-$. Gibbs free energies at 0 K [$\Delta E(\text{electronic}) + \Delta ZPE$, left] and 600 K (right); BSSE-corrected. The energy scales are offset to 0 kcal mol⁻¹ for $[P(N_3)_6]^-$ as the reference.

change of the total energy of $-10 \text{ kcal mol}^{-1}$ (B3LYP and BSSE-corrected). While reassociation of the N_3^- ligand has a nearly barrierless energy profile, reassociation of N_2 has to overcome a substantial reaction barrier of 57 kcal mol^{-1} (B3LYP). Searches for the accurate transition state geometries in *Gaussian09* were guided by evaluation of the reaction coordinates described earlier.

In order to single out the thermodynamically preferred reaction path and allow for a direct comparison with the simulations, thermal Gibbs free energies (G) were calculated for optimized structures of reaction products and starting complexes as well as for transition states. According to the Gibbs free energies of individual structures in DFT at $T = 0 \text{ K}$ (B3LYP, Figure 6), N_2 elimination is the thermodynamically preferred reaction (path 3). However, the free-energy reaction barrier estimated by TS3 ($43.9 \text{ kcal mol}^{-1}$) is approximately the same as the free energy required for N_3^- dissociation ($44.2 \text{ kcal mol}^{-1}$), while the free reaction energy for path 3 is small and negative ($-14 \text{ kcal mol}^{-1}$). Intriguingly, the free-energy barrier (TS3) falls only slightly to 42 kcal mol^{-1} for calculations at 600 K , while the free reaction energy required for N_3^- dissociation reduces substantially to 22 kcal mol^{-1} . An increase of the temperature increases the thermodynamic preference for N_2 elimination from -14 to $-37 \text{ kcal mol}^{-1}$, and the transition state for N_2 elimination is lowered only slightly in free energy with respect to $[\text{P}(\text{N}_3)_6]^-$. However, dissociation of an N_3 ligand as N_3^- requires much less free energy at 600 K than at 0 K and is therefore tentatively assigned as the initial process operational at high temperature. These findings are in accordance with the molecular dynamics simulations, which showed dissociation to $\text{P}(\text{N}_3)_5$ and N_3^- exclusively at this temperature on the singlet surface. The preference for either reaction path depends on the temperature and is controlled by a large difference in the entropy of dissociation of N_3^- ($35 \text{ cal mol}^{-1} \text{ K}^{-1}$) and the entropy of activation accompanying the formation of the transition state for dissociation of N_2 ($4 \text{ cal mol}^{-1} \text{ K}^{-1}$). The energetics are to some extent dependent on the functional and method. While the total energy changes for path 3 range from $+1.3 \text{ kcal mol}^{-1}$ (MP2) to $-9.7 \text{ kcal mol}^{-1}$ (RM06HF) and for path 1 from 54 kcal mol^{-1} (B3LYP) to 62 kcal mol^{-1} (MP2), RM06HF and MP2 find large energy penalties for path 2 of 91 and 98 kcal mol^{-1} , respectively. These data suggest that N_3^\bullet elimination from $[\text{P}(\text{N}_3)_6]^-$ is less likely even at high temperature. Furthermore, promoting $^1[\text{P}(\text{N}_3)_6]^-$ to $^3[\text{P}(\text{N}_3)_6]^-$ requires ca. 53 kcal mol^{-1} (B3LYP). $^3[\text{P}(\text{N}_3)_6]^-$ has a much smaller reaction barrier toward N_2 elimination in comparison with the closed-shell species (2.0 vs $46.8 \text{ kcal mol}^{-1}$; see Table S18 in the SI). The involvement of open-shell species can be assessed by determination of the minimum-energy crossing point,⁵¹ which may be the subject of future investigation.

Onset of Irreversible Decomposition. Given that the thermally activated reaction of $[\text{P}(\text{N}_3)_6]^-$ affording $\text{P}(\text{N}_3)_5$ and N_3^- is fully reversible (in the gas phase), the onset of irreversible decomposition (pyrolysis) can occur indirectly in a secondary reaction step involving $[\text{P}(\text{N}_3)_5]$. Using the same technique as that for the penta(azido)phosphosphate $[\text{P}(\text{N}_3)_5]$, total energy profiles were obtained for the reactions (1a) and (1b) involving dissociation in $[\text{P}(\text{N}_3)_4]^+$ and N_3^- and elimination of N_2 , respectively (Figure 7, Scheme 3). The calculations show that at 600 K dissociation of N_3^- from $\text{P}(\text{N}_3)_5$ requires free-energy changes of $+113 \text{ kcal mol}^{-1}$ (B3LYP) and $+94 \text{ kcal mol}^{-1}$ (BLYP). Elongation of the $\text{P}-$

N_α bond causes at first a change of the trigonal-bipyramidal coordination geometry to a seesaw type involving a shared negative charge between $\text{P}(\text{N}_3)_4$ and the N_3 fragment. At a $\text{P}-\text{N}_\alpha$ distance larger than ca. 2.9 \AA , $\text{P}(\text{N}_3)_4$ adopts a tetrahedral arrangement of ligands characteristic of $[\text{PX}_4]^+$ complexes. The released N_3 ligand is anionic and the geometry of the $\text{P}(\text{N}_3)_4$ fragment resembles closely the geometry of $[\text{P}(\text{N}_3)_4]^+$ obtained from an independent geometry optimization using the same method and functional. The release of N_2 from $[\text{P}(\text{N}_3)_5]$ has a comparatively low free-energy reaction barrier in comparison to N_3^- , of only 26 kcal mol^{-1} (B3LYP). The lone N_α atom left behind by the loss of the N_2 fragment inserts into an adjacent $\text{P}-\text{N}_\alpha$ bond, forming the η^1 -coordinating chainlike N_4 ligand also encountered in the release of N_2 from $[\text{P}(\text{N}_3)_6]^-$. The reverse reaction has a large free-energy barrier of ca. 70 kcal mol^{-1} (B3LYP).

An assessment of the energetics for paths 2 and 2a (Scheme 3 and Figure 6) is more difficult because the search for a transition state needs to take into account the separation of spins. Unrestricted DFT calculations on the B3LYP/6-311G-(d,p) level of theory suggest that, provided the radical species $[\text{P}(\text{N}_3)_5]^-$ is accessible via a low-lying transition state, the free-energy reaction barrier for N_2 elimination would be higher than that for $[\text{P}(\text{N}_3)_5]$.

The release of N_3^- from $[\text{P}(\text{N}_3)_4]^+$ was not evaluated further because the required energy exceeds $100 \text{ kcal mol}^{-1}$, rendering this reaction pathway energetically unfavorable by far in comparison with N_2 elimination from $[\text{P}(\text{N}_3)_6]^-$, $[\text{P}(\text{N}_3)_5]$, or $[\text{P}(\text{N}_3)_5]^-$. [Using the equation $[\text{P}(\text{N}_3)_6]^- \rightarrow [\text{P}(\text{N}_3)_2]^- + 6\text{N}_2$, an upper limit for the total enthalpy of decomposition of $[\text{P}(\text{N}_3)_6]^-$ can be estimated to be less than $-234 \text{ kcal mol}^{-1}$. This value compares well with the results of differential scanning calorimetry measurements of the salt $[(\text{PPh}_3)_2\text{N}][\text{P}(\text{N}_3)_6]$, the first decomposition step of which has an enthalpy change of $-226 \text{ kcal mol}^{-1.5}$]

CONCLUSIONS

The results provide support for the empirical rule predicting that the propensity for N_2 release from an azide compound increases with a reduction of the ionic character of the element– N_3 bond. The temperature appears to have a decisive influence on the initial reaction pathway on the singlet surface. At 0 K , removal of N_3^- requires only as much free energy as is required to overcome the free-energy barrier for N_2 elimination. At 600 K , the energetics are ca. 20 kcal mol^{-1} in favor of N_3^- elimination. Depending on the method and temperature, the calculations on the singlet surface show a free-energy reaction barrier for N_2 release from $[\text{P}(\text{N}_3)_5]$ that is 10 – 18 kcal mol^{-1} below that of $[\text{P}(\text{N}_3)_6]^-$. Thus, $[\text{P}(\text{N}_3)_6]^-$ is expected to be less prone to N_2 release than the pentacoordinate, neutral $[\text{P}(\text{N}_3)_5]$, which contains $\text{P}-\text{N}_\alpha$ bonds of lesser polarity. We have shown that AIMD simulations can be used to obtain insight into the thermally activated reactions of nitrogen-rich energetic complexes on the example of $[\text{P}(\text{N}_3)_6]^-$. On the singlet surface, the simulations revealed the reversible dissociation of the complex to the penta(azido)phosphorane $[\text{P}(\text{N}_3)_5]$ and the azido anion N_3^- . The complex $[\text{P}(\text{N}_3)_5]$ performs a pseudorotation of the Berry type, giving first insight into this phenomenon operating in homoleptic polyazides. DFT, HF, and MP2 calculations all reveal a decrease of the free energy of the dissociated state $\{[\text{P}(\text{N}_3)_5] + \text{N}_3^-\}$ relative to $[\text{P}(\text{N}_3)_6]^-$ upon an increase in the temperature from 0 to 600 K . This effect of the temperature renders the ionic $[\text{P}(\text{N}_3)_6]^-$ less

accessible to N₂ release in favor of the formation of covalent [P(N₃)₅], which prepares irreversible N₂ release. The energy profiles, referring to hypothetical reactions at T = 0, for N₂ elimination and initial N₃⁻ dissociation, followed by N₂, as determined by DFT calculations predict that N₂ elimination is the thermodynamically preferred process, which is, however, disfavored kinetically. This indicates a strong dependence of the overall dissociation path on the working temperature and is consistent with the results of the dynamical simulations, which show direct N₃⁻ dissociation at T = 600 and T = 1200 K. The precise extent of involvement of open-shell species is a subject for future investigation.

■ ASSOCIATED CONTENT

■ Supporting Information

Further information on the AIMD simulations with time steps of 0.48 fs (Tables S1–S6 and Figure S1) and 0.24 fs (Scheme S1, Tables S7–S14, and Figures S2–S5) and AIMD simulations with fixed N_α–N_β distances; coordinates, energies, frequencies, and thermal corrections; and a full description of the material. This material is available free of charge via the Internet at <http://pubs.acs.org>.

■ AUTHOR INFORMATION

Corresponding Author

*E-mail: carmen.domene@chem.ox.ac.uk (C.D.), p.portius@sheffield.ac.uk (P.P.). Tel: +44 (0) 1865 285110 (C.D.), +44 (0)114 22 29385 (P.P.). Fax: +44 (0) 1865 275674 (C.D.), +44 (0)114 22 29346 (P.P.).

Notes

The authors declare no competing financial interest.

■ ACKNOWLEDGMENTS

C.D. thanks The Royal Society for a University Research Fellowship. This work made use of the Oxford Supercomputer Center (OSC) and the UK national high-performance computing service facilities (HECToR) provided by UoE HPCx Ltd. at the University of Edinburgh, Cray Inc., and NAG Ltd. by the Engineering and Physical Sciences Research Council's (EPSRC) High End Computing Programme. P.P. thanks the EPSRC for an Advanced Research Fellowship (EP/E054978/1).

■ REFERENCES

- (1) Banert, K.; Joo, Y.-H.; Rüffer, T.; Walfort, B.; Lang, H. *Angew. Chem., Int. Ed.* **2007**, *46*, 1168.
- (2) Portius, P.; Filippou, A. C.; Schnakenburg, G.; Davis, M.; Wehrstedt, K.-D. *Angew. Chem., Int. Ed.* **2010**, *49*, 8013.
- (3) Fränk, W.; Habereeder, T.; Hammerl, A.; Klapötke, T. M.; Krumm, B.; Mayer, P.; Nöth, H.; Warchhold, M. *Inorg. Chem.* **2001**, *40*, 1334.
- (4) Sussek, H.; Stowasser, F.; Pritzkow, H.; Fischer, R. A. *Eur. J. Inorg. Chem.* **2000**, *3*, 455.
- (5) Portius, P.; Fowler, P. W.; Adams, H.; Todorova, T. Z. *Inorg. Chem.* **2008**, *47*, 12004.
- (6) Klapötke, T. M.; Nöth, H.; Schütt, T.; Warchhold, M. *Angew. Chem., Int. Ed.* **2000**, *39*, 2108.
- (7) Lyhs, B.; Jansen, G.; Bläser, D.; Wölper, C.; Schulz, S. *Chem.—Eur. J.* **2011**, *17*, 11394.
- (8) Filippou, A. C.; Portius, P.; Schnakenburg, G. *J. Am. Chem. Soc.* **2002**, *124*, 12396.
- (9) Filippou, A. C.; Portius, P.; Neumann, D. U.; Wehrstedt, K.-D. *Angew. Chem., Int. Ed.* **2000**, *39*, 4333.

- (10) Fenske, D.; Dörner, H. D.; Dehnicke, K. Z. *Naturforsch., B: Chem. Sci.* **1983**, *38*, 1301.
- (11) Polborn, K.; Leidl, E.; Beck, W. Z. *Naturforsch., B: Chem. Sci.* **1988**, *43*, 1206.
- (12) Klapötke, T. M.; Krumm, B.; Scherr, M.; Haiges, R.; Christe, K. O. *Angew. Chem., Int. Ed.* **2007**, *46*, 8686.
- (13) Haiges, R.; Boatz, J. A.; Vij, A.; Gerken, M.; Schneider, S.; Schroer, T.; Christe, K. O. *Angew. Chem., Int. Ed.* **2003**, *42*, 5847.
- (14) Portius, P.; Davis, M. *Coord. Chem. Rev.* **2012**.
- (15) Abramovitch, R. A.; Kyba, E. P. *J. Am. Chem. Soc.* **1974**, *96*, 480.
- (16) Besora, M.; Harvey, J. N. *J. Chem. Phys. A* **2008**, *129*, 839.
- (17) Bock, H.; Dammel, R.; Horner, L. *Chem. Ber.* **1981**, *114*, 220.
- (18) Odell, M. S.; Darwent, B. D. *Can. J. Chem.* **1970**, *48*, 1140.
- (19) Troe, J.; Wagner, H. G. *Annu. Rev. Phys. Chem.* **1972**, *23*, 311.
- (20) Arenas, J. F.; Marcos, J. I.; Lopez-Tocon, I.; Otero, J. C.; Soto, J. *J. Chem. Phys.* **2000**, *113*, 2282.
- (21) Arenas, J. F.; Marcos, J. I.; Otero, J. C.; Tocon, I. L.; Soto, J. *Int. J. Quantum Chem.* **2001**, *84*, 241.
- (22) Alexander, M. H.; Werner, H. J.; Hemmer, T.; Knowles, P. J. *J. Chem. Phys.* **1990**, *93*, 3307.
- (23) Foy, B. R.; Casassa, M. P.; Stephenson, J. C.; King, D. S. *J. Chem. Phys.* **1989**, *90*, 7037.
- (24) Göbel, M.; Karaghiosoff, K.; Klapötke, T. M. *Angew. Chem., Int. Ed.* **2006**, *45*, 6037.
- (25) Arenas, J. F.; Otero, J. C.; Sanchez-Galvez, A.; Soto, J.; Viruela, P. *J. Phys. Chem. A* **1998**, *102*, 1146.
- (26) Bock, H.; Dammel, R. *Angew. Chem., Int. Ed. Engl.* **1987**, *26*, 504.
- (27) Odell, M. S.; Darwent, B. D. *Can. J. Chem.* **1970**, *48*, 1140.
- (28) Bock, H.; Dammel, R. *Angew. Chem.* **1985**, *97*, 128.
- (29) Fau, S.; Wilson, K. J. *J. Phys. Chem. A* **2002**, *106*, 4639.
- (30) Fau, S.; Bartlett, R. J. *Theor. Comput. Chem.* **2003**, *12*, 441.
- (31) Dixon, D. A.; Feller, D.; Christe, K. O.; Wilson, W. W.; Vij, A.; Vij, V.; Jenkins, H. D. B.; Olson, R. M.; Gordon, M. S. *J. Am. Chem. Soc.* **2004**, *126*, 834.
- (32) Portius, P.; Filippou, A. C.; Schnakenburg, G.; Davis, M.; Wehrstedt, K. D. *Angew. Chem., Int. Ed.* **2010**, *49*, 8013.
- (33) Portius, P.; Fowler, P. W.; Adams, H.; Todorova, T. Z. *Inorg. Chem.* **2008**, *47*, 12004.
- (34) Scriven, E. F. V.; Turnbull, K. *Chem. Rev.* **1988**, *88*, 297.
- (35) Hobbs, K. R.; Coombe, R. D. *Thin Solid Films* **2002**, *402*, 162.
- (36) Linnen, C. J.; Macks, D. E.; Coombe, R. D. *J. Phys. Chem. B* **1997**, *101*, 1602.
- (37) Zhu, H. L.; Han, F. D.; Bi, J. Q.; Bai, Y. J.; Qi, Y. X.; Pang, L. L.; Wang, C. G.; Li, S. J.; Lu, C. W. *J. Am. Ceram. Soc.* **2009**, *92*, 535.
- (38) Becke, A. D. *Phys. Rev. A* **1988**, *38*, 3098.
- (39) Lee, C. T.; Yang, W. T.; Parr, R. G. *Phys. Rev. B* **1988**, *37*, 785.
- (40) CPMD Copyright IBM Corp., 1990–2004. Copyright MPI fuer Festkoerperforschung Stuttgart, 1997–2001.
- (41) Goedecker, S.; Teter, M.; Hutter, J. *Phys. Rev. B* **1996**, *54*, 1703.
- (42) Hartwigsen, C.; Goedecker, S.; Hutter, J. *Phys. Rev. B* **1998**, *58*, 3641.
- (43) Nose, S.; Klein, M. L. *Mol. Phys.* **1983**, *50*, 1055.
- (44) Hockney, R. W. *Methods Comput. Phys.* **1970**, *9*, 136.
- (45) Sprik, M.; Ciccotti, G. *J. Chem. Phys.* **1998**, *109*, 7737.
- (46) Frisch, M. J.; et al. *Gaussian09*; Gaussian Inc.: Wallingford, CT, 2009.
- (47) Berry, R. S. *J. Chem. Phys.* **1960**, *32*, 933.
- (48) Haiges, R.; Boatz, J. A.; Vij, A.; Gerken, M.; Schneider, S.; Schroer, T.; Christe, K. O. *Angew. Chem., Int. Ed.* **2003**, *42*, 5847.
- (49) Workentin, M. S.; Wagner, B. D.; Negri, F.; Zgierski, M. Z.; Luszytk, J.; Siebrand, W.; Wayner, D. D. M. *J. Phys. Chem.* **1995**, *99*, 94.
- (50) Zhao, Y.; Truhlar, D. G. *J. Phys. Chem. A* **2006**, *110*, 13126.
- (51) Chachiyo, T.; Rodriguez, J. H. *J. Chem. Phys.* **2005**, *123*.